

# Design and optimisation of a low-cost titanium dioxide-coated stainless steel mesh photocatalytic water treatment reactor



Matthieu Grao, Marina Ratova\*, Peter Kelly

Department of Engineering, Faculty of Science and Engineering, Manchester Metropolitan University, Chester Street, Manchester, M1 5GD, UK

## ARTICLE INFO

### Article history:

Received 21 April 2020

Received in revised form

10 February 2021

Accepted 4 March 2021

Available online 10 March 2021

Handling editor: Bin Chen

### Keywords:

Photocatalysis

Water treatment reactor

Titanium dioxide

Magnetron sputtering

Design of experiments

Stainless steel mesh

## ABSTRACT

Photocatalysis has been extensively studied in recent years for environmental wastewater treatment applications. Although promising, it has yet to be globally adopted, as it faces many challenges; namely cost, complexity and efficiency. This present work focuses on the optimisation of a bespoke photocatalytic water treatment reactor. Contrary to other studies, the reactor was exclusively built from inexpensive and readily available consumer market parts, to facilitate a widespread adoption of this water treatment method. Photocatalytic TiO<sub>2</sub> was synthesised and immobilised on stainless steel woven mesh in a one-step process, via reactive pulsed DC magnetron sputtering. A two-levels augmented screening design template was used to optimise the performance of the bespoke photocatalytic reactor, consisting of 20 experimental runs. Five independent variables were studied, UV light intensity, number of TiO<sub>2</sub>-coated mesh layers, coating thickness, water flowrate and initial dye concentration. Methylene blue dye solution was used as a model pollutant and the removal percentage after 5 h was used as a response. A linear regression model was built from the experimental results and revealed that all first-order terms, with the exception of flowrate, were significant contributors to the model pollutant removal. Increasing the coating thickness and the number of TiO<sub>2</sub>-coated mesh layers did improve the removal rate of methylene blue. These benefits cancelled each other when both variables were at their highest levels, due to a decreased light permeability through the mesh. ANOVA, lack-of-fit, and R<sup>2</sup> analysis confirmed the significance of the linear regression model. Optimised conditions were identified, leading to the removal of more than 90% of the model pollutant after 5 h of UV-A illumination. The calculated pseudo-first-order constant was as high as  $14.5 \times 10^{-5} \text{ s}^{-1}$ , while the quantum yield was estimated to be  $4.22 \times 10^{-6}$  molecules/photons and the figure of merit was calculated at 1.14. This substrate/catalyst combination proved to be effective at degrading methylene blue, with no evident performance degradation after 10 repeated cycles, equivalent to 360 h of consecutive use. This present work demonstrates that it is possible to build an efficient photocatalytic reactor from inexpensive computer enthusiast parts, combined with a highly scalable and industry friendly photocatalyst production technique.

© 2021 Elsevier Ltd. All rights reserved.

## 1. Introduction

According to the data published by the World Health Organization (WHO), in 2017 almost a third of the global population did not have access to safely managed, available and uncontaminated drinking-water services (World Health Organization, 2019). It is predicted that by 2025, half of the world's population will be living

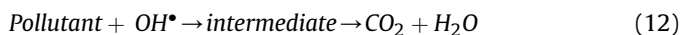
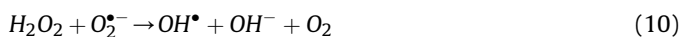
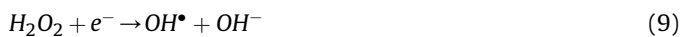
in water stressed areas. Use and consumption of unsanitary water is known to result in rapid spread of diarrhoea, cholera, dysentery, typhoid, and polio; thriving and praying on the most vulnerable populations. In the near future, water scarcity and imbalance is predicted to be one of the many consequences of climate change (Anser et al., 2020; Zhao et al., 2019; Zhu et al., 2020).

To address this pressing issue, environmentally friendly and sustainable processes must be developed and implemented to treat unsanitary water. Photocatalysis could be the answer, as it only requires a photocatalyst and an appropriate light source to operate. This advanced oxidation process (AOP) involves the absorption of photons of sufficient energy, by a semiconductor photocatalyst, to

\* Corresponding author. Department of Engineering, Manchester Metropolitan University, John Dalton Building, Chester Street, Manchester M1 5GD, UK.

E-mail addresses: [marina\\_ratova@hotmail.com](mailto:marina_ratova@hotmail.com), [m.ratova@mmu.ac.uk](mailto:m.ratova@mmu.ac.uk) (M. Ratova).

promote valence band electrons to the conduction band and form electron-hole pairs (equation (1)). These charge carriers diffuse to the photocatalyst's surface, react with water and oxygen molecules to form highly reactive radical species, through a series of chain reactions, as described by equations (2)–(11) (Fatima et al., 2019). These radical species progressively oxidise organic pollutants into less harmful intermediate products, until complete mineralisation is achieved (equation (12)).



The most widely used photocatalyst is crystalline titanium dioxide (TiO<sub>2</sub>), whose photocatalytic properties were discovered by Fujishima and Honda in 1969 (Fujishima and Honda, 1972). It is non-toxic, stable, inexpensive and has been extensively used for water electrolysis, dye-sensitised solar cells, air/water purification, self-cleaning coatings, self-cleaning glass, self-sterilising coatings, etc. (Byrne et al., 2018). Photocatalysts are most commonly studied in powder form, where they generally possess higher activity than thin films, but they then require post-treatment separation to safely discharge the treated water. This major drawback limits the scalability and widespread adoption of powder-based photocatalytic water treatment systems. Efforts were made to use immobilised photocatalysts, as they do not require any post-treatment separation, but their effectiveness can be limited by mass and photon transfer. These limitations can be mitigated when catalyst thickness, reactant proximity, catalyst surface area and light permeability are considered carefully (Sundar and Kanmani, 2020).

In his critical review, Juan José Rueda-Marquez identified several barriers, which hinder the development of real world photocatalytic water treatment applications (Rueda-Marquez et al., 2020):

- Most studies are performed on a laboratory scale.
- There is a lack of attention given to photocatalyst reusability.
- More than 60% of studies are performed on powders.

- Upfront and operational water treatment cost are rarely included.

This study aims at addressing some of the points raised by Rueda-Marquez et al., by building and optimising a photocatalytic reactor, made with inexpensive components and loaded with stainless steel mesh coated with TiO<sub>2</sub> thin films. The upfront and operating cost of this proof of concept were both included in this study, while the reusability was assessed for 360 h of consecutive use.

Practical use of photocatalytic materials for water and wastewater treatment can be facilitated through their integration into so-called photocatalytic reactors. Although there is a wide variety of reactor types (fluidized bed, optical fibre monolith, micro-channel, annular etc.), they usually share common features, such as the presence of a reactor vessel, a light source, a photocatalyst and a form of solution agitator. Photocatalytic reactors aimed towards wastewater treatment can generally be classified in two categories: slurry type and immobilised type. Regardless of the chosen type, the main attributes of an ideal photocatalytic reactor should be the following (Colmenares and Xu, 2016): high quantum efficiency, high catalyst specific surface area, efficient mass transfer, low cost and low toxicity. To enable efficient transfer from a laboratory environment to real-world applications, the photocatalyst manufacturing process should be scalable and the reactor components should be inexpensive.

It is common practice for free form photocatalysts to be immobilised by spray coating (Cortes et al., 2019; Lasa et al., 2005), which involves slurry preparation, air spraying and calcination steps. In an earlier study, 304 stainless steel mesh was successfully coated with photocatalytic TiO<sub>2</sub>, in a one-step process, demonstrated its efficiency against a range of model pollutants and identified O<sub>2</sub><sup>•-</sup> and OH<sup>•</sup> as the photocatalytic reaction's main driving force (Grao et al., 2020). The photocatalyst was deposited by reactive magnetron sputtering, in a one-step process, which represents a significant time and economic gain, especially for high volume manufacturing, compared to multi-step chemical techniques. Magnetron sputtering is reproducible, highly scalable and provides excellent control over chemical and morphological properties (Kelly and Arnell, 2000). This stainless-steel mesh substrate was chosen for its inexpensiveness, flexibility, durability and, importantly, ability to let light pass through. Layers of stainless-steel woven mesh can be stacked in a photocatalytic reactor, increasing the catalyst load whilst maintaining light permeability. TiO<sub>2</sub> coated stainless steel mesh was integrated in a bespoke photocatalytic reactor, LCPR-I (Low-Cost Photocatalytic Reactor-I). Key parameters were optimised to maximise the reactor's efficiency, based on its ability to degrade a model pollutant; methylene blue (MB). Five parameters were varied along an augmented screening design template to identify the most important parameters and optimise the process: UV-A light intensity, number of TiO<sub>2</sub>-coated mesh layers, coating thickness, water flowrate and initial dye concentration.

This reactor fabrication process did not involve any expensive components (glass, quartz, membranes, air injector etc.) and it was almost exclusively built from components available in an everyday computer store, making this system easily accessible and affordable. The photocatalyst deposition process is scalable, reproducible and already widely established in high volume manufacturing processes. The combined affordability, simplicity and efficiency of this proof of concept represents a sustainable option to treat wastewater and help to bridge the gap between materials research and real-world applications.

## 2. Materials and methods

### 2.1. Deposition process

Titanium dioxide thin films were deposited in a single-stage process in a Nordiko sputtering rig (Fig. 1), under a high vacuum, achieved through a combination of rotary (BOC Edwards 80) and turbo molecular (Leybold TMP1000) pumps. A single directly cooled 300 × 100 mm titanium target (99.5% purity) was fitted onto a Gencoa Ltd unbalanced type II magnetron. The distance between the target and the substrate was kept at 50 mm for all deposition runs. The argon flow rate was kept constant at 50 sccm for all deposition runs. The oxygen flow was regulated by a Speedflo<sup>®</sup>™ controller from Gencoa Ltd., to produce stoichiometric TiO<sub>2</sub> films and to minimise target poisoning. The magnetron was powered by an Advanced Energy Pinnacle Plus power supply in pulsed DC mode operating at a power of 2 kW, frequency of 100 kHz and 60% duty. The coatings were deposited for either 1 or 2 h onto 15 × 12.5 and 15 × 9 cm<sup>2</sup> sheets of stainless steel 304 mesh, with a 0.223 mm aperture and a wire diameter of 0.14 mm (purchased from the Mesh Company, Warrington, UK); the substrate was ultrasonically pre-cleaned in acetone prior to deposition. All chemicals used were purchased from Sigma Aldrich, unless stated otherwise.

### 2.2. Characterisation

The thin film morphology was evaluated by scanning electron microscopy (SEM) using a Zeiss Supra 40 VP-FEG-SEM. The deposited film thicknesses were estimated from their cross-sectional SEM micrographs. The crystallinity of the coatings was assessed by X-ray diffraction (XRD), on a Panalytical Xpert system, with CuK<sub>α1</sub> radiation at 0.154 nm, in grazing incidence mode at 3°

angle of incidence over a scan range from 20 to 70° (2θ), the accelerating voltage and applied current were 40 kV and 30 mA, respectively. The optical band gap of the TiO<sub>2</sub> coatings on mesh substrates was estimated using the Tauc plot method (Tauc et al., 1966), by measuring the optical absorbance of TiO<sub>2</sub> coatings on soda lime glass slides produced under the same conditions. The absorbance spectrum and corresponding Tauc plot are given in supplementary materials (S1).

### 2.3. Photocatalytic performance assessment

The photocatalytic performances of the bespoke water treatment reactor were assessed by monitoring its ability to degrade methylene blue under UV-A light. The reactor was loaded with TiO<sub>2</sub> coated mesh and filled with an aqueous methylene blue (purchased from Alfa Aesar) solution of 500 mL at a concentration of either 1 or 5 μmol.L<sup>-1</sup>. The reactor was left in the dark at room temperature for 12 h under continuous solution circulation to reach adsorption-desorption equilibrium. Once reached, the UV-A source (Sankyo Denki BLB lamps, peak output at 365 nm) was powered up for 24 h. The methylene blue main absorption peak at 664 nm was monitored every 1 h with an Ocean Optics USB4000 UV–visible spectrometer. Between each test, both the coated mesh sheets and the reactor were thoroughly rinsed with distilled water. The reactor's photocatalytic degradation efficiency was calculated using equation (13) and used as a response to optimise the photocatalytic degradation process, with A<sub>0</sub> and A<sub>t</sub> as MB's main absorbance peak at 0 and 5 h of UV irradiation, respectively. The pseudo-first-order rate constant (k<sub>a</sub>), quantum yield (QY) and figure of merit (FOM) were calculated as performance metrics for the best photocatalytic reactor configuration (run No. 16). The pseudo-first-order rate was obtained by plotting Ln(A<sub>0</sub>/A<sub>t</sub>) against time and calculating the

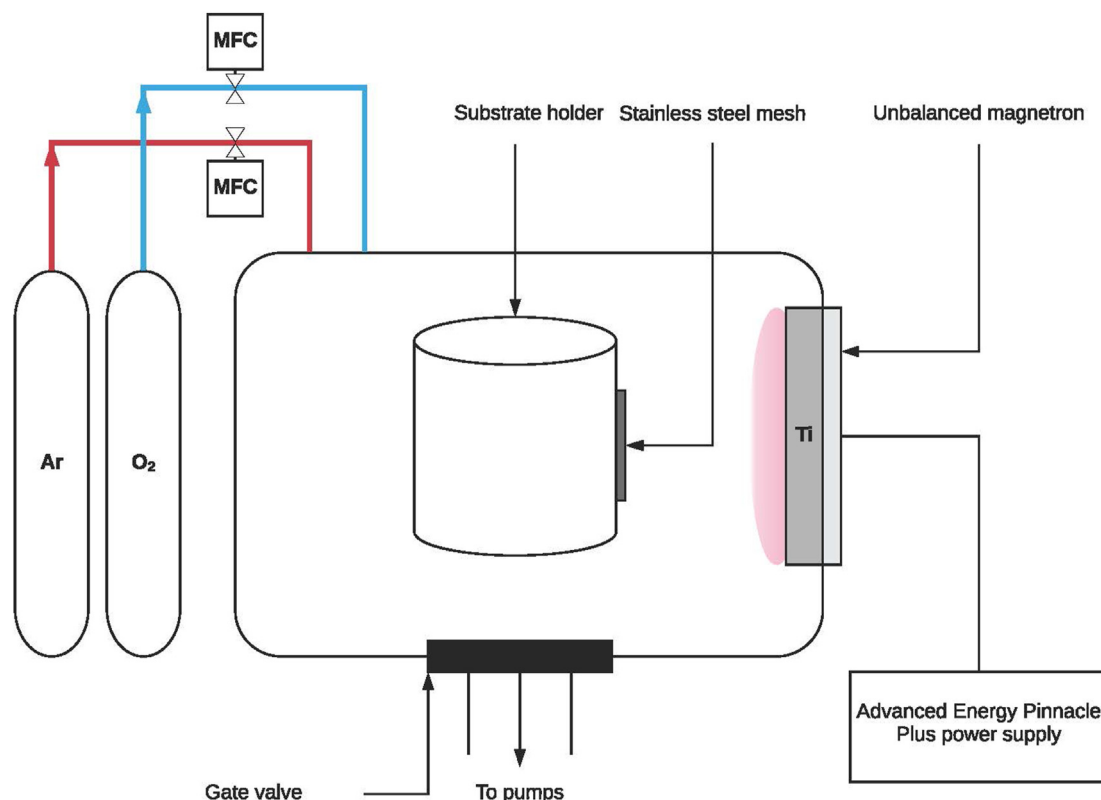


Fig. 1. Schematic representation of the Nordiko sputtering rig.

plot's gradient. QY is used as a metric to quantify how effectively a semiconductor can utilise absorbed photons to decompose a pollutant, it was obtained using equation (14), with  $r$  ( $\text{mol}\cdot\text{cm}^{-2}\cdot\text{s}^{-1}$ ) the reaction rate and  $\phi$  ( $\text{mol}\cdot\text{cm}^{-2}\cdot\text{s}^{-1}$ ) the flux of absorbed photons (He et al., 2020). The figure of merit is a performance indicator which takes into account the volume of treated solution, the amount of catalyst, the treatment time and the energy consumption of the system. FOM was calculated using equation (15) and graded between 0 and 100 using a conversion factor used to index 85 different photocatalytic systems (Anwer et al., 2019).

$$MB_{\text{removal}}(\%) = \frac{A_0 - A_t}{A_0} \times 100 \quad (13)$$

$$QY = \frac{\text{number of reacted molecules}}{\text{number of absorbed photons}} = \frac{r}{\phi} \quad (14)$$

$$FOM = \frac{\text{Product obtained (L)}}{\text{Catalyst dosage (g}\cdot\text{L}^{-1}) \times \text{Time (h)} \times \text{Energy consumption (Wh}\cdot\mu\text{mol}^{-1})} \quad (15)$$

The photon flux was obtained by integrated irradiance measurement, from 300 to 410 nm, with a USB4000 UV–visible spectrometer from Ocean Optics. Due to the photocatalyst's wide bandgap (3.2 eV), it is assumed that wavelengths over 410 nm cannot excite electrons from the valence to the conduction band. To obtain an estimation of the number of absorbed photons, irradiance measurements were performed by drilling a hole in the middle of the reactor and inserting the optic fibre in the MB filled reactor after 2.5 h of reaction, with and without the coated mesh. The irradiance measurement spectra are provided in supplementary materials (S2).

#### 2.4. Durability and reusability assessment

To evaluate the durability and reusability of the coated mesh, 10 consecutive MB removal tests were performed with the most efficient configuration (run No. 16), using the same photocatalytic activity assessment apparatus. A small square of  $0.25\text{ cm}^2$  was cut from the coated mesh sample, to verify the thin film's integrity by Raman mapping analysis. Afterwards, the sample was soldered back to its original position, for further testing and the operation was repeated 2 additional times. Raman mapping was performed after the 1st, 5th and 10th tests using a DXR Raman microscope from Thermo Scientific. The Raman spectra were analysed over a range of  $100\text{--}1000\text{ cm}^{-1}$  and the Raman maps were constructed

**Table 1**  
Deposition conditions and characteristics of the two coating types.

Deposition parameters	Condition 1	Condition 2	Units
Deposition time	1	2	h
Power	2	2	kW
Frequency	100	100	kHz
Base pressure	0.3	0.3	( $10^{-2}$ ) Pa
Working pressure	44	44	( $10^{-2}$ ) Pa
Gas	Ar/O <sub>2</sub>	Ar/O <sub>2</sub>	–
Distance <sub>target-substrate</sub>	5	5	cm
<b>Characterisation</b>			
Crystalline phase(s)	Anatase	Anatase + Rutile	–
Thickness	$1.1 \pm 0.1$	$1.6 \pm 0.1$	$\mu\text{m}$

using the integrated intensities of the main anatase peak at  $144\text{ cm}^{-1}$  (Ohsaka et al., 1978). The laser was operated at a wavelength of 532 nm, with a power of 10 mW, 900 lines per mm grating, a long working distance (LWD) microscope objective with magnification of  $\times 50$ , an estimated spot size of  $1.1\text{ }\mu\text{m}$  and a  $25\text{ }\mu\text{m}$  pinhole. 10201 Raman spectra were acquired per analysis, using a step size of  $50\text{ }\mu\text{m}$  along the Y and X axes.

### 3. Results

#### 3.1. Coating deposition and characterisation

Stainless steel 304 woven mesh was coated with TiO<sub>2</sub> by pulsed DC reactive magnetron sputtering in a single-step process at ambient temperature. To evaluate the impact of coating thickness on the reactor's photocatalytic capabilities, two deposition times were used, 1 and 2 h. Table 1 summarises the conditions used to obtain these two types of coatings and their respective character-

istics. The coatings obtained at the two deposition times were examined by FEG-SEM and their top view and cross-sectional micrographs are given in Fig. 2. The top view of the two conditions revealed a dense microstructure with crystal-like features, as shown in Fig. 2(A, C). An analysis of the samples' cross-section, in Fig. 2(B, D), highlighted the columnar aspects of the coatings. This might be a result of the angled deposition of TiO<sub>2</sub> on the curved surface of the stainless-steel substrate, which could promote columnar growth through shadowing effects. Average thicknesses of  $1.1 \pm 0.1$  and  $1.6 \pm 0.1\text{ }\mu\text{m}$  were measured for the 1 and 2 h depositions, respectively.

The XRD analysis of the TiO<sub>2</sub> coated mesh revealed the presence of well-defined diffraction peaks, corresponding to crystalline TiO<sub>2</sub> for both deposition times (Fig. 3). Diffraction peaks at  $44.42^\circ$  (111),  $51.58^\circ$  (200),  $75.48^\circ$  (220) were identified as austenite stainless steel using the JCPDS card 00-003-0397, arising from the substrate material. The diffraction pattern of the 1 h deposition (Fig. 3(A)) revealed anatase diffraction peaks at  $25.35^\circ$  (101),  $37.93^\circ$  (004) and  $38.61^\circ$  (112) identified with the JCPDS card 96-720-6076. After 2 h of deposition (Fig. 3 (B)), anatase  $25.35^\circ$  (101),  $37.93^\circ$  (004),  $38.61^\circ$  (112),  $48.10^\circ$  (200),  $53.89^\circ$  (105),  $55.29^\circ$  (211) and rutile diffraction peaks at  $54.32^\circ$  (211),  $62.74^\circ$  (002) were identified with the JCPDS cards 96-720-6076 and 96-900-4145, respectively.

For both deposition times, crystalline titanium dioxide structures were obtained in a one-step process without any thermal treatment. Increasing the coating's thickness gave rise to new anatase diffraction peaks and to the appearance of an additional rutile phase. Anatase and rutile mixtures are known to have an enhanced photocatalytic activity compared to each polymorph on its own (Bickley et al., 1991). This rutile and anatase mixture could result in an increase photocatalytic activity for the 2 h deposition samples.

#### 3.2. Photocatalytic reactor design

The LCPR-I design inspiration can be traced to the Photo-CREC-Water I, developed at the Chemical Reactor Engineering Centre

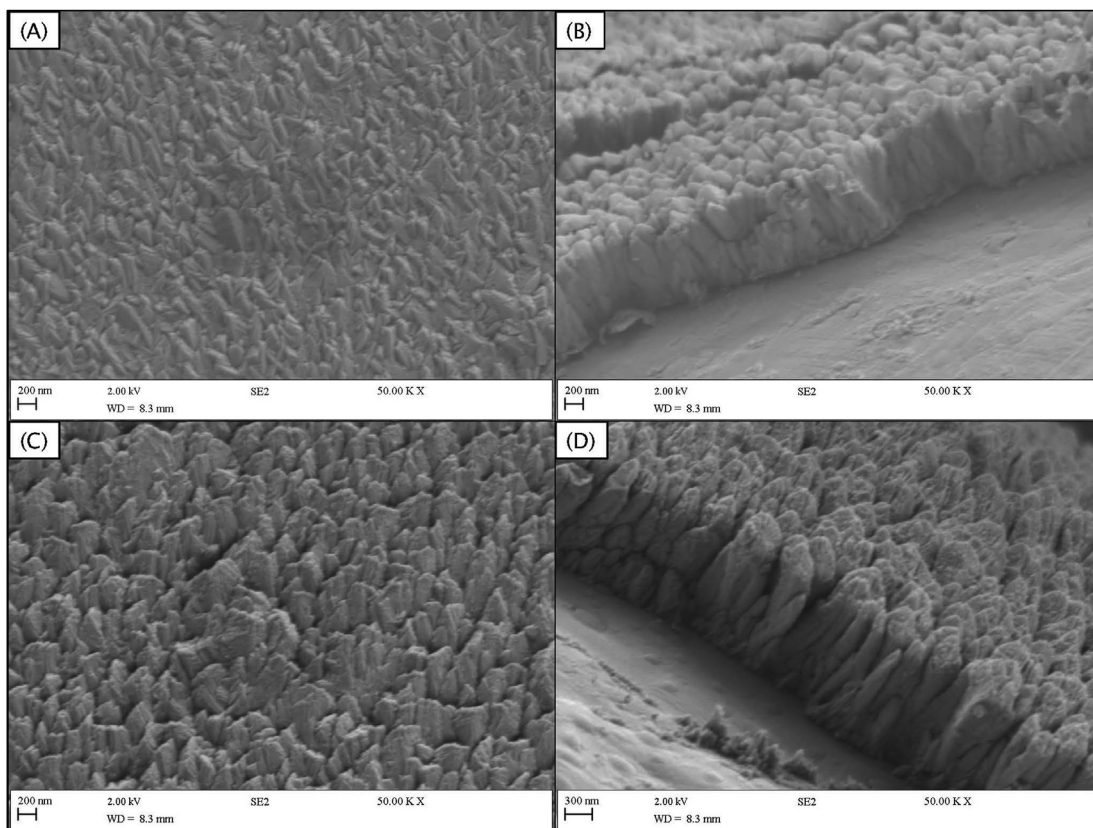


Fig. 2. FEG-SEM micrographs of the TiO<sub>2</sub> coated mesh samples; (A) 1 h deposition top-view; (B) 1 h deposition cross-section; (C) 2 h deposition top-view; (D) 2 h deposition cross-section.

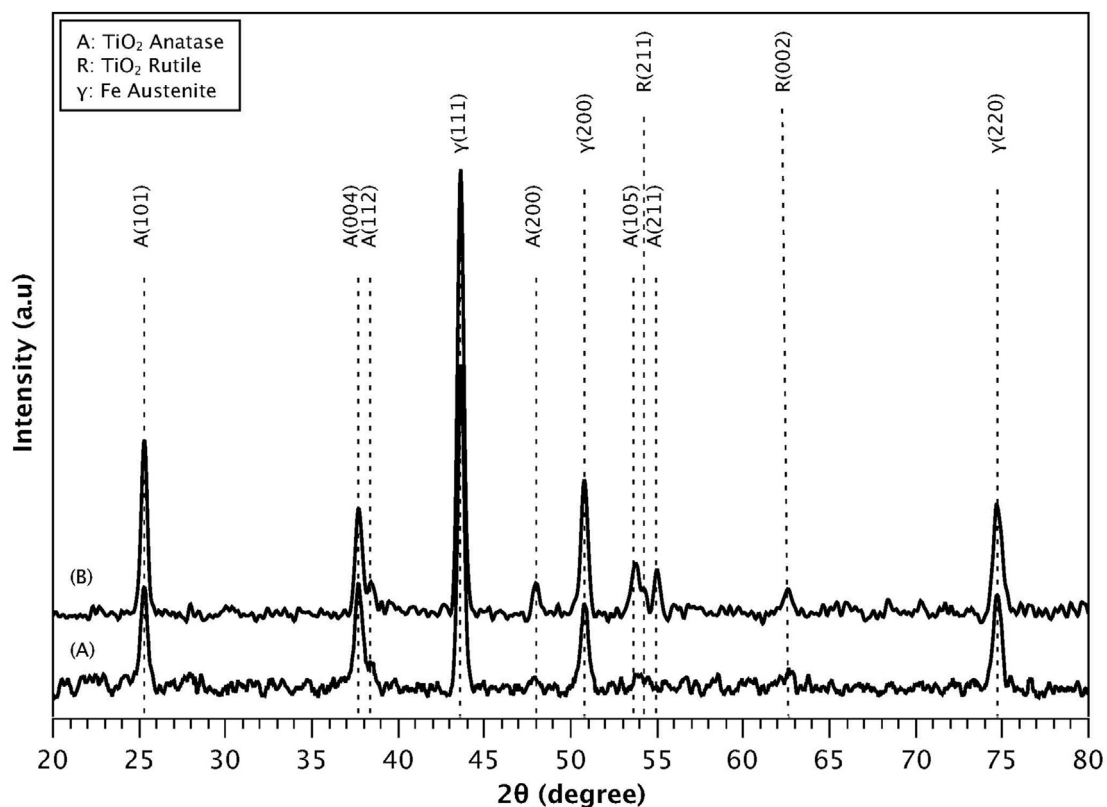


Fig. 3. XRD analysis of the TiO<sub>2</sub>-coated mesh samples; (A) 1 h deposition; (B) 2 h deposition.

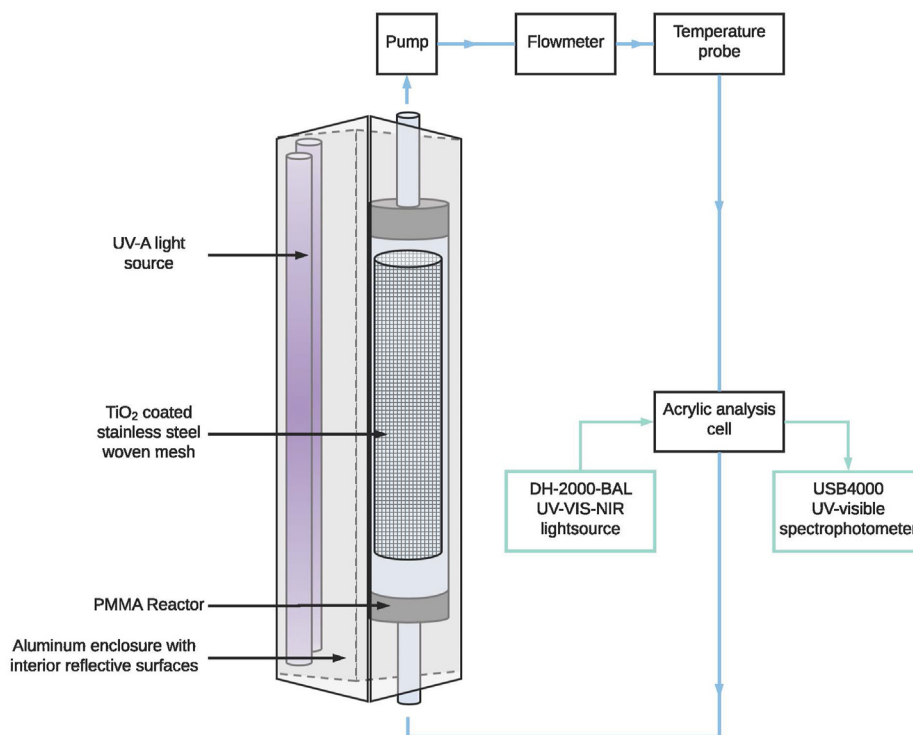


Fig. 4. Schematic representation of LCPR-I utilising TiO<sub>2</sub>-coated stainless-steel mesh.

(CREC) of the University of Western Ontario, by Lasa et al. (2005). Likewise, the catalyst was immobilised on stainless steel mesh, albeit using another immobilisation technique, and the reactor was operated in batch mode. Unlike Photo-CREC-Water I, this bespoke reactor utilises an external light source and does not involve quartz or glass components, significantly reducing the system’s cost and increasing its durability. With the exception of the UV-A lamps, the set-up was built exclusively from affordable and readily available components, purchased from the computer enthusiast market. Fig. 4 provides a schematic representation of the bespoke water treatment photocatalytic reactor loaded with TiO<sub>2</sub>-coated stainless-steel mesh photocatalyst.

In brief, the system is comprised of a cylindrical reactor made from PMMA (OD: 5 cm, h: 24 cm), transparent PVC tubing (OD: 16 mm, ID: 10 mm), a 12 V pump, a flowmeter, a temperature probe and an acrylic analysis cell. The reactor was placed in an aluminium enclosure with a UV-A irradiation source, detailed in Section 2.3. Depending on the design matrix experiment, either 1 × 15 W or 2 × 15 W light bulbs were used, the pump’s voltage was varied between 6 and 12 V to adjust the flowrate. The reactor was loaded with either 15 × 12.5 cm<sup>2</sup> or 15 × 12.5 + 15 × 9 cm<sup>2</sup> cylinder(s) of stainless steel 304 sheets of mesh, coated on both sides with TiO<sub>2</sub>

Table 2  
Experimental ranges and levels of the independent operating variables.

Variables	Symbol	Unit	Range and levels	
			-1	+1
UV light	X <sub>1</sub>	W	15	30
Number of TiO <sub>2</sub> -coated mesh layers	X <sub>2</sub>	–	1	2
Coating thickness	X <sub>3</sub>	Mm	1.1	1.6
Flowrate	X <sub>4</sub>	L.min <sup>-1</sup>	5.14	9.54
Initial dye concentration	X <sub>5</sub>	µmol.L <sup>-1</sup>	1	5
Uncontrollable variables: Temperature (K) and Power consumption (W)				

with varying thickness levels. A full breakdown of the upfront price of the LCPR-I is given in supplementary data (S3).

### 3.3. Design of experiments

The independent variables used for this design of experiments array are presented in Table 2, including corresponding levels and coding. The augmented screening design was constructed and analysed using the JMP 14 SW statistical software from SAS. The studied variables were UV light intensity (W) (X<sub>1</sub>), number of TiO<sub>2</sub>-coated mesh layers (X<sub>2</sub>), coating thickness (µm) (X<sub>3</sub>), flow rate (L min<sup>-1</sup>) (X<sub>4</sub>), and initial dye concentration (µmol.L<sup>-1</sup>) (X<sub>5</sub>); these variables were varied along two levels; low (-1) and high (+1); all variable parameters were chosen to be within operational range of the proposed reactor and therefore, no design modifications were required. Noise factors, namely, temperature (K) and power consumption (W) were also recorded during each experiment. Although temperature is known to positively influence photocatalytic reactions (Gupta et al., 2012; Hu et al., 2010; Yamamoto et al., 2013); the measured variations were considered too low to have a significant impact (Table 3). Z. Shams-Ghahfarokhi et al. reported an increased decolorization efficiency at higher temperatures, with significant improvements only occurring above 333 K (Shams-Ghahfarokhi and Nezamzadeh-Ejhih, 2015). The power drawn by the system was measured directly at the wall with a wattmeter. Power consumption varied from 37 to 67 W, depending on the levels of the independent operating variables (Table 3). The pH values of the media were measured before and after each experiment; this value was 6, regardless of variable experimental parameters, therefore, was not discussed further in work progression. To assess the contribution of photolysis, a run termed No. 0 was performed with two sets of uncoated mesh, 1 µmol.L<sup>-1</sup> of initial dye concentration and 30 W UV light. Photolysis seemed to account for less than 10% of the dye degradation after 5 h of UV irradiation.

**Table 3**  
Design matrix for the 5 tested independent variables with the experimental and predicted responses.

Run No.	X <sub>1</sub>	X <sub>2</sub>	X <sub>3</sub>	X <sub>4</sub>	X <sub>5</sub>	MB removal (%)		Uncontrollable variables	
						Experimental	Predicted	Temperature (K)	Power drawn (W)
0	+1	-	-	- 1	- 1	9.9	-	299	53
1	+1	+1	- 1	- 1	+1	64.8	60.8	300	54
2	-	- 1	+1	+1	+1	45.2	43.8	300	50
3	-	+1	- 1	+1	+1	36.4	44.0	300	49
4	+1	- 1	- 1	- 1	+1	37.6	44.3	300	53
5	-	+1	+1	- 1	- 1	61.3	70.8	298	37
6	+1	- 1	- 1	+1	- 1	72.4	72.6	303	67
7	-	- 1	- 1	+1	- 1	54.9	55.8	299	50
8	+1	+1	+1	+1	- 1	82.5	87.6	303	67
9	+1	+1	+1	+1	+1	58.4	59.3	306	66
10	-	+1	- 1	- 1	- 1	73.2	72.3	300	37
11	+1	- 1	+1	- 1	- 1	88.7	89.0	300	54
12	-	- 1	+1	- 1	+1	37.0	43.8	298	38
13	+1	+1	- 1	+1	+1	60.1	60.8	303	66
14	+1	- 1	+1	- 1	+1	70.3	60.6	300	53
15	-	+1	+1	+1	- 1	77.6	70.8	300	49
16	+1	+1	- 1	- 1	- 1	<b>93.0</b>	<b>89.2</b>	<b>300</b>	<b>54</b>
17	-	- 1	- 1	+1	+1	26.8	27.4	300	37
18	+1	- 1	+1	+1	- 1	85.2	89.0	302	67
19	-	- 1	- 1	- 1	- 1	64.1	55.8	297	37
20	-	+1	+1	- 1	+1	52.1	42.4	296	38

The two-levels design matrix with the corresponding experimental and predicted results for each statistical combination of independent variables are displayed in Table 3. The predicted values were obtained by fitting a regression model to the experimental data, to determine the optimal operating conditions. Regression coefficients were determined to develop a regression model, based on significant main or interaction effects. In the case of a 2-levels experiment, the regression coefficients are calculated by dividing the estimates of effects  $E_f$  by 2. A regression model (16) can then be designed, with  $\hat{y}$  as the predicted response,  $\beta_0$  as the intercept,  $\beta_i$  as a regression coefficient,  $\beta_{ij}$  as the interaction

**Table 4**  
Parameter estimates for significant independent variables and 2nd order interactions.

Term	Estimate (%)	Std Error (%)	t-ratio	p-value
Intercept	62.0	1.5	42.3	<0.0001
X <sub>1</sub>	8.4	1.5	5.6	<0.0001
X <sub>2</sub>	3.8	1.5	2.6	0.0212
X <sub>3</sub>	3.7	1.5	2.5	0.0242
X <sub>5</sub>	-14.2	1.5	-9.5	<0.0001
X <sub>2</sub> X <sub>3</sub>	-4.4	1.5	-2.9	0.0112

(X<sub>1</sub>) UV light; (X<sub>2</sub>) number of TiO<sub>2</sub>-coated mesh layers; (X<sub>3</sub>) Coating thickness; (X<sub>4</sub>) Flowrate; (X<sub>5</sub>) Initial dye concentration.

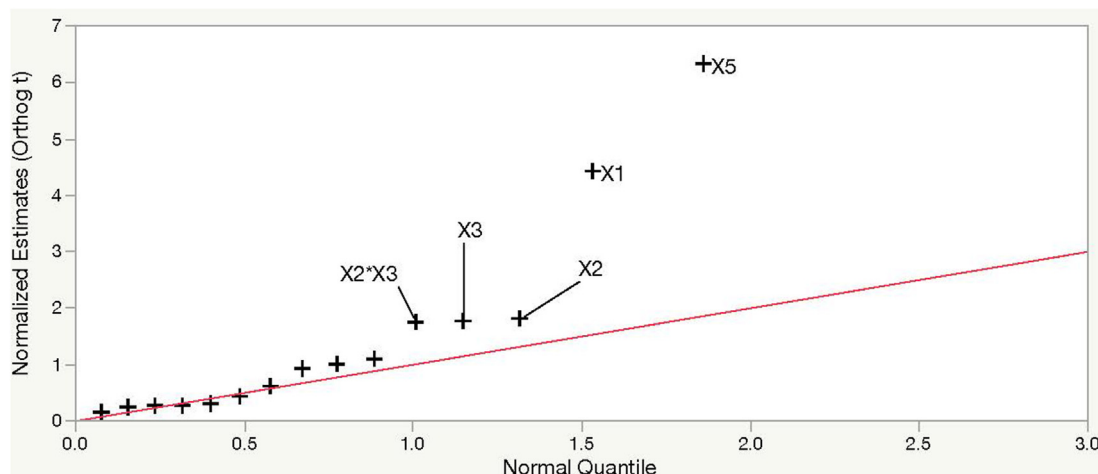


Fig. 5. Half-normal plot for all independent variables and 2nd order interactions.

**Table 5**  
Analysis of variance (ANOVA) and Lack-of-fit (LOF) for MB removal efficiency of the TiO<sub>2</sub>-coated stainless-steel mesh-based photoreactor.

Source	DF	Sum of Squares	Mean Square	F Ratio	p-value
Model	5	0.620	0.124	28.895	<0.0000
Error	14	0.060	0.004		
C. Total	19	0.680			
Lack of fit	9	0.036	0.004	0.850	0.610
Pure error	5	0.024	0.005		
Total error	14	0.060			

$R_{squared} = 0.9117$ ,  $Adjusted\ R_{squared} = 0.8801$

between the process parameters  $X_i$  and  $X_j$ , and ‘ $\epsilon$ ’ as the random error component.

$$\hat{y} = \beta_0 + \beta_1 X_1 + \beta_2 X_2 + \dots + \beta_{12} X_1 X_2 + \beta_{12} X_1 X_2 + \dots + \epsilon \quad (16)$$

Using a backward selection method, a regression model was generated with all factors and 2nd order interactions (Bruce and Bruce, 2017). Statistically significant independent variables and 2nd order interactions were identified using a half-normal plot. This graphical tool uses estimated effects to visually assess the significance of factor(s) and interaction(s) (Daniel, 1959). Insignificant factors or interactions should fall along a straight line, while significant one’s should form outliers. As displayed in Fig. 5, initial dye concentration ( $X_5$ ), UV light intensity ( $X_1$ ), number of TiO<sub>2</sub>-coated mesh layers ( $X_2$ ), coating thickness ( $X_3$ ) and the interaction between coating thickness and number of TiO<sub>2</sub>-coated mesh layers ( $X_2 X_3$ ) seem to stand out as significant. Flowrate does not seem to play any significant role in the MB removal, suggesting that the lowest selected level is appropriate, and that mass transfer does not bottleneck the reaction. The parameter estimates report (Table 4) presents the significance and direction of the chosen parameters and interaction, with their associated t-ratios and p-values. All selected parameters have an absolute t-ratio greater than 1.96 and p-values smaller than 0.05, confirming the statistically significance of their effects.

Statistically non-significant predictors were successively taken away from the model until only statistically significant ones remained. Using the parameter estimates, the following regression model (17), was designed to predict MB removal percentage, after 5 h, by the TiO<sub>2</sub>-coated mesh reactor.

$$\hat{y} = 62 + 8.4 \times X_1 + 3.8 \times X_2 + 3.7 \times X_3 - 14.2 \times X_5 - 4.4 \times X_2 X_3 \quad (17)$$

The quality of the fit for this model was assessed using an analysis of variance (ANOVA), presented in Table 5. The F-ratio was used to assess whether the designed model differed significantly from a model where all predicted values are equal to the response mean. If the null hypothesis is true, the F-ratio should be close to 1, i.e. the chosen parameters do not describe accurately the actual data variations (Dougherty, 2011; Nguyen et al., 2019). The associated p-values measured the probability of obtaining a F-ratio, as large as the one observed, with all parameters set to zero except the intercept. Small p-values (<0.05) would indicate that the observed large F-ratio is unlikely to be obtained by pure chance alone and that the null hypothesis can be rejected. The large F-ratio (28.895) and small p-value (<0.0000), obtained with the ANOVA confirm that the model describes accurately the data variations and that the chosen parameters are significant.

Besides, the accuracy of fit between the experimental values and the model was assessed by analysing the lack-of-fit (LOF) (Nguyen et al., 2019). The regression model fits the experimental data well, as the mean square of the lack-of-fit error (0.004) was close to the pure error (0.005). The lack-of-fit for this model was statistically insignificant with a large p-value (0.610) and a F-ratio close to 1 (0.850), confirming that this model can be used for both prediction and optimisation.

The model’s goodness-of-fit was confirmed by the  $R^2$  (0.91) and  $R^2_{adjusted}$  (0.88) for experimental data points plotted against the predicted values (Montgomery, 2008). The  $R^2_{adjusted}$  is a modified version of  $R^2$  which takes into account the model’s number of predictors. The small gap between  $R^2$  (0.91) and  $R^2_{adjusted}$  (0.88) indicates that the experimental data variations are in accordance with the model and that the predicted responses are trustworthy (Table 5). Plotting the data against the predicted responses (Fig. 6(A)) highlighted the agreement of the model with the experimental values. The normal probability plot of the residuals, shown in Fig. 6(B), approximately forms a straight line, supporting the assumptions that the error terms are normally distributed.

Overall, the analysis of variance, lack of fit, and  $R^2$  results all confirmed that the model was statistically significant and could be used to predict and optimise the % removal of MB after 5 h using the TiO<sub>2</sub>-coated mesh photocatalytic reactor.

### 3.4. Durability and reusability assessment

The best set of conditions (sample No. 16), predicted by the model and verified experimentally, was used to assess the reusability potential of the TiO<sub>2</sub>-coated stainless-steel mesh. As

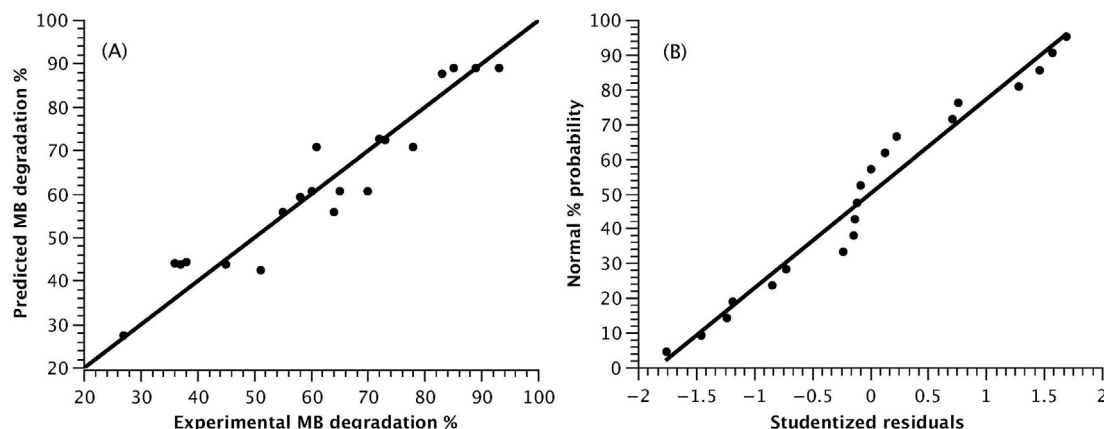


Fig. 6. Diagnostic plots for the photocatalytic MB removal % after 5 h: (A) Experimental by predicted plot; (B) Normal probability plot of residuals.

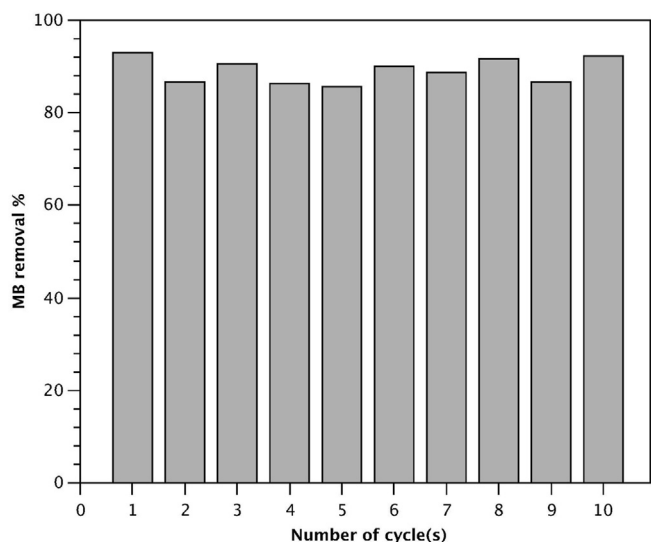


Fig. 7. Reusability assessment of the TiO<sub>2</sub>-coated mesh; MB removal percentage after 5 h for 10 consecutive cycles.

displayed in Fig. 7, no apparent reduction in photocatalytic activity was observed after 10 consecutive cycles or 360 h of testing. In

Fig. 8, the Raman mapping confirmed this trend, with no obvious change in the coating's integrity being observed between the first analysis and after 180 and 360 h of testing. The visual differences observed in Fig. 8(D) are due to the bending of the sample in certain areas (mainly lower left) after multiple handlings, while performing repeated analysis. This bending of the mesh resulted in out of focus analysis, which is why some threads appear bare whilst other apertures appear coated.

#### 4. Discussion

The influence of five parameters was investigated for their role in the removal of methylene blue after 5 h, in this bespoke photocatalytic reactor. Using a linear regression model, UV light intensity (X<sub>1</sub>), number of TiO<sub>2</sub>-coated mesh layers (X<sub>2</sub>), coating thickness (X<sub>3</sub>) and initial dye concentration (X<sub>5</sub>) were identified as the most important and influential parameters. Flowrate (X<sub>4</sub>) had no effect on the MB removal rate, at the minimum (5.14 L min<sup>-1</sup>) and maximum (9.54 L min<sup>-1</sup>) operating conditions of the 12 V pump. This is consistent with the findings of de Lasa et al. who concluded that mass transfer was not limiting the removal of MB in their photocatalytic reactor, for flowrates equal or higher than 1.7 L min<sup>-1</sup> (Lasa et al., 2005). Decreasing the initial dye concentration (X<sub>5</sub>) resulted in an increased MB removal rate, which could be the result of a lower consumption of radical species by

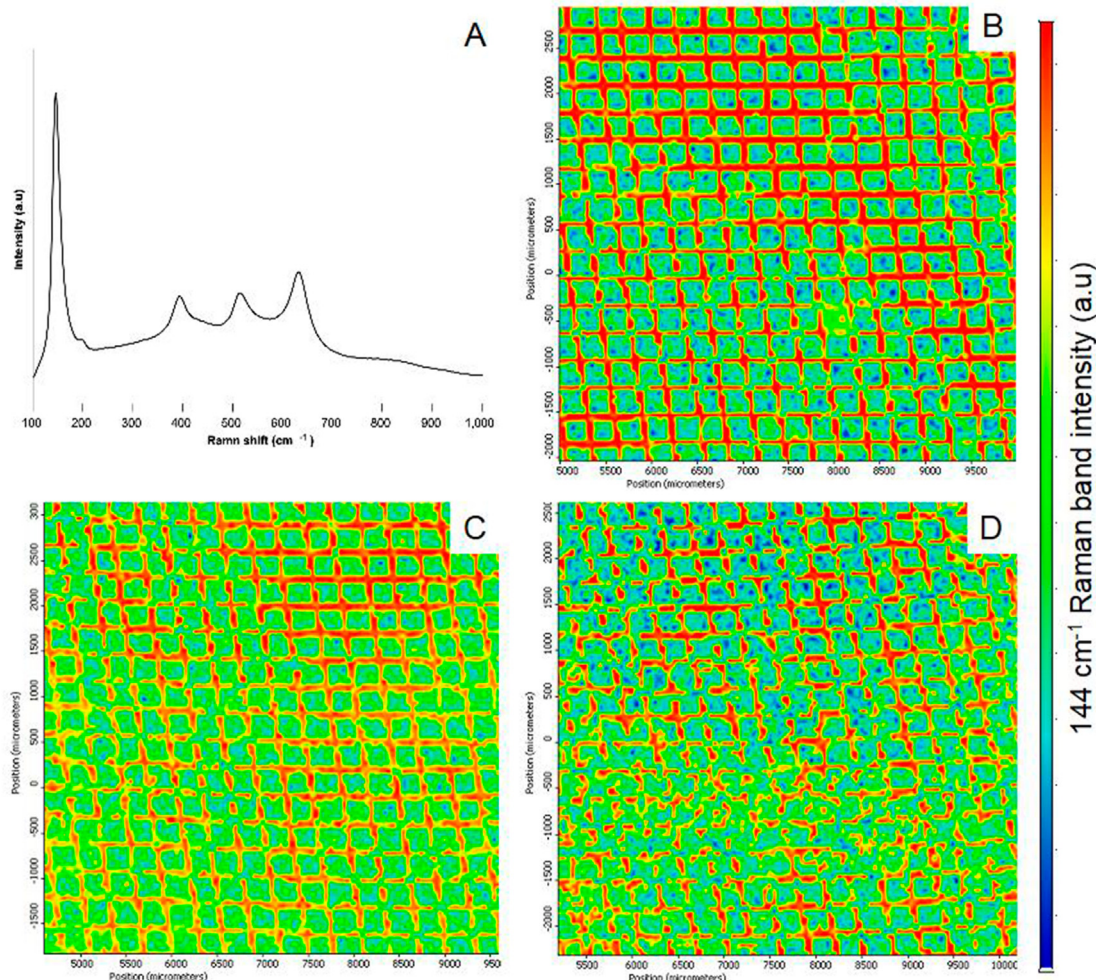
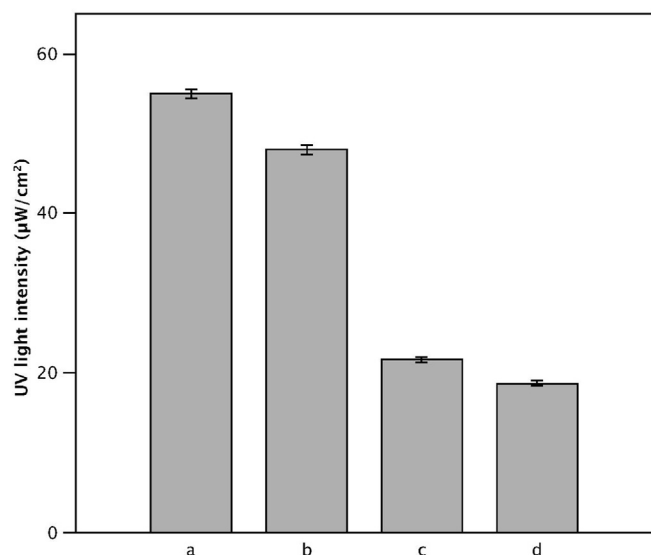


Fig. 8. Raman maps with integrated intensities of (A) the main anatase peak at 144 cm<sup>-1</sup> of the same area after the (B) 1st, (C) 5th and (D) 10th MB degradation cycle.



**Fig. 9.** UV light intensity measured for different mesh configurations; (a) 1 set of mesh, 1 h deposition; (b) 1 set of mesh, 2 h deposition; (c) 2 sets of mesh, 1 h deposition; (d) 2 sets of mesh, 2 h deposition.

intermediary products (Ahmed et al., 2011; Ajmal et al., 2014). Increasing the UV light intensity ( $X_1$ ) improved the MB removal, as it is known to increase the photogeneration of excitons and of radical species (Ajmal et al., 2014; Cassano and Alfano, 2000; Chen et al., 2007). Increasing the coating thickness ( $X_3$ ) and the number of  $\text{TiO}_2$ -coated mesh layers ( $X_2$ ) also improved the MB removal rate. The former has been reported as having a positive effect on photocatalytic activity, with significant improvements occurring between 100 and 500 nm, and to a lesser extent between 500 nm and 2  $\mu\text{m}$  (Davíðsdóttir et al., 2014). Increasing the latter comes down to increasing the catalyst load, which is known to improve the reaction rate (Yunus et al., 2017). Interestingly, a significant negative interaction between the coating thickness ( $X_3$ ) and the number of  $\text{TiO}_2$ -coated mesh layers ( $X_2$ ) seemed to play a role in the MB removal efficiency. Overlapping two sets of mesh coated with  $\text{TiO}_2$  for 2 h could hinder light permeability, in turn decreasing the efficiency of the system. It was confirmed experimentally, by measuring the UV light intensity (at 365 nm) received by a UVP UVX Radiometer detector, after passing through the reactor loaded with different mesh configurations (Fig. 9). Decreases of 12.7 and 13.8% were observed, respectively, for one and two sets of coated stainless-steel mesh, when the coating thickness increased from 1.1

to 1.6  $\mu\text{m}$ . These values are only indicative, as the measurements were performed without the reflective surfaces.

The characteristics and performance metrics of this bespoke reactor are summarised in Table 6. The LCPR-I displayed rather average QY and FOM levels. This can be explained by the composition of the reactor walls (PMMA), which absorbed >80% of incident UV-A light, as shown in supplementary materials. Despite this limited UV-A transmittance, LCPR-I still managed to achieve a FOM of 1.14, achieving better performance than >40% of the 85 systems reviewed by Anwer et al. (2019). It should be noted though, that as a metric, the FOM parameter tends to favour powder-form photocatalysts, due to the “catalyst dosage” component used in equation (15). Specific surface area is known to be positively correlated with photocatalytic activity (Amano et al., 2010), which is negligible when comparing powder-form photocatalysts of similar specific surface area. This is not the case for immobilised photocatalysts, as photocatalytic reactions only occur on the film’s exposed surface, which is orders of magnitude smaller than their powder counterpart. This is especially true for thin films produced by reactive magnetron sputtering, which tend to form dense columnar structures (Kelly and Arnell, 2000).

Whilst the results of the current study are encouraging, there is still room for improvement for this proof of concept. The interaction between coating thickness and the number of  $\text{TiO}_2$ -coated mesh layers was identified as having a negative impact on the MB removal efficiency. To increase the catalyst load whilst maintaining light permeability, different strategies can be implemented, such as simultaneously irradiating the reactor from different angles and/or using different mesh aperture sizes.

Future work will be aimed at coating the LCPR-I mesh, using reactive magnetron sputtering, with a sunlight-activated photocatalyst, instead of  $\text{TiO}_2$ , and evaluating its effectiveness against micro-organisms, pharmaceuticals and real-world wastewater samples. Fouling was not investigated in this study due to the use of deionised water, but it will be in future work, as microbial presence in wastewater would produce biofouling and affect the photo-reactor’s performance. Using sunlight not only would reduce the upfront cost of the system by over 60%, but it would considerably reduce the amount of irradiation absorbed by the reactor walls, resulting in more efficient water-treatment performance.

## 5. Conclusions

In this study, a bespoke photocatalytic reactor (LCPR-I) was built from low cost consumer market parts and used to degrade a model pollutant, methylene blue. The reactor utilises crystalline  $\text{TiO}_2$ -coated woven stainless-steel mesh photocatalyst, produced in a

**Table 6**  
Summary of reactor characteristics.

Parameters	Unit	LCPR-I
Catalyst	–	$\text{TiO}_2$
Optical bandgap	eV	3.2
Synthesis method	–	Pulsed DC Reactive Magnetron sputtering
Coating thickness	Mm	1.6
Pollutant	–	Methylene blue
Catalyst loading	$\text{g.L}^{-1}$	0.34
Initial concentration	$\mu\text{mol.L}^{-1}$	1
Light power (peaked at 365 nm)	$\text{mW/cm}^2$	6.2
Degradation efficiency after 5 h of UV-A irradiation	%	93
Power consumption	$\text{Wh.}\mu\text{mol}^{-1}$	627
Flux of absorbed photons ( $\phi$ )	$10^{-8} \text{ mol cm}^{-2}.\text{s}^{-1}$	1.90
Reaction rate ( $r$ )	$10^{-14} \text{ mol cm}^{-2}.\text{s}^{-1}$	8.01
Quantum yield (QY)	$10^{-6} \text{ molecule.photon}^{-1}$	4.22
*Figure of merit (FOM)	$\mu\text{mol.Wh}^{-1}.\text{h}^{-1}.\text{g}^{-1}$	1.14

\*FOM classification: best (100), good (30–10), average (10–1) and below average (<1).

one-step process by reactive pulsed DC magnetron sputtering. This deposition process is sustainable and addresses the technical viability and economic feasibility challenges faced by photocatalytic waste treatment. The methylene blue removal percentage after 5 h was optimised by investigating the influence of UV light intensity, number of TiO<sub>2</sub>-coated mesh layers, coating thickness and water flowrate. All factors, with the exception of flowrate, were found to have an influence on the removal process efficiency. 30 W UV-A, 2 layers of mesh coated with 1.1 μm of TiO<sub>2</sub> and a flowrate of at least 5.14 L min<sup>-1</sup> were found to be the optimum conditions, leading to the removal of more than 90% of the model pollutant under 5 h. The coated stainless-steel woven mesh has proven to be durable as the photocatalytic activity of the material remained unchanged after 360 h of consecutive use. The findings of this study, as well as the proposed reactor design, may be of considerable interest for those involved in practical implementation of sustainable and efficient photocatalytic water treatment processes.

### CRediT authorship contribution statement

**Matthieu Grao:** Conceptualization, Methodology, Software, Validation, Investigation, Writing – original draft, Writing – review editing, Visualization. **Marina Ratova:** Conceptualization, Validation, Writing – original draft, Writing – review editing, Supervision, Project administration. **Peter Kelly:** Resources, Writing – original draft, Writing – review editing, Supervision, Funding acquisition. All authors have read and agreed to the published version of the manuscript.

### Declaration of competing interest

The authors declare that they have no known competing financial interests or personal relationships that could have appeared to influence the work reported in this paper.

### Appendix A. Supplementary data

Supplementary data to this article can be found online at <https://doi.org/10.1016/j.jclepro.2021.126641>.

### References

- Ahmed, S., Rasul, M.G., Brown, R., Hashib, M.A., 2011. Influence of parameters on the heterogeneous photocatalytic degradation of pesticides and phenolic contaminants in wastewater: a short review. *J. Environ. Manag.* 92, 311–330. <https://doi.org/10.1016/j.jenvman.2010.08.028>.
- Ajmal, A., Majeed, I., Malik, R.N., Idriss, H., Nadeem, M.A., 2014. Principles and mechanisms of photocatalytic dye degradation on TiO<sub>2</sub> based photocatalysts: a comparative overview. *RSC Adv.* 4, 37003–37026. <https://doi.org/10.1039/C4RA06658H>.
- Amano, F., Nogami, K., Tanaka, M., Ohtani, B., 2010. Correlation between surface area and photocatalytic activity for acetaldehyde decomposition over bismuth tungstate particles with a hierarchical structure. *Langmuir* 26, 7174–7180. <https://doi.org/10.1021/la904274c>.
- Anser, M.K., Yousaf, Z., Usman, B., Nassani, A.A., Qazi Abro, M.M., Zaman, K., 2020. Management of water, energy, and food resources: go for green policies. *J. Clean. Prod.* 251, 119662 <https://doi.org/10.1016/j.jclepro.2019.119662>.
- Anwer, H., Mahmood, A., Lee, J., Kim, K.-H., Park, J.-W., Yip, A.C.K., 2019. Photocatalysts for degradation of dyes in industrial effluents: opportunities and challenges. *Nano Res* 12, 955–972. <https://doi.org/10.1007/s12274-019-2287-0>.
- Bickley, R.L., Gonzalez-Carreño, T., Lees, J.S., Palmisano, L., Tilley, R.J.D., 1991. A structural investigation of titanium dioxide photocatalysts. *J. Solid State Chem.* 92, 178–190. [https://doi.org/10.1016/0022-4596\(91\)90255-G](https://doi.org/10.1016/0022-4596(91)90255-G).
- Bruce, P., Bruce, A., 2017. *Practical Statistics for Data Scientists: 50 Essential Concepts*. O'Reilly Media, Inc.
- Byrne, C., Subramanian, G., Pillai, S.C., 2018. Recent advances in photocatalysis for environmental applications. *J. Environ. Chem. Eng.* 6, 3531–3555. <https://doi.org/10.1016/j.jece.2017.07.080>.
- Cassano, A.E., Alfano, O.M., 2000. Reaction engineering of suspended solid heterogeneous photocatalytic reactors. *Catal. Today* 58, 167–197. [https://doi.org/10.1016/S0920-5861\(00\)00251-0](https://doi.org/10.1016/S0920-5861(00)00251-0).
- Chen, J.-Q., Wang, D., Zhu, M.-X., Gao, C.-J., 2007. Photocatalytic degradation of dimethoate using nanosized TiO<sub>2</sub> powder. *Desalination* 207, 87–94. <https://doi.org/10.1016/j.desal.2006.06.012>.
- Colmenares, J.C., Xu, Y.-J. (Eds.), 2016. *Heterogeneous Photocatalysis: from Fundamentals to Green Applications*, Green Chemistry and Sustainable Technology. Springer-Verlag, Berlin Heidelberg.
- Cortes, M.A.L.R.M., Hamilton, J.W.J., Sharma, P.K., Brown, A., Nolan, M., Gray, K.A., Byrne, J.A., 2019. Formal quantum efficiencies for the photocatalytic reduction of CO<sub>2</sub> in a gas phase batch reactor. *Catalysis Today*, SI: Proc PSS2017 326, 75–81. <https://doi.org/10.1016/j.cattod.2018.10.047>.
- Daniel, C., 1959. Use of half-normal plots in interpreting factorial two-level experiments. *Technometrics* 1, 311–341. <https://doi.org/10.1080/00401706.1959.10489866>.
- Davidsdóttir, S., Shabadi, R., Galca, A.C., Andersen, I.H., Dirscherl, K., Ambat, R., 2014. Investigation of DC magnetron-sputtered TiO<sub>2</sub> coatings: effect of coating thickness, structure, and morphology on photocatalytic activity. *Appl. Surf. Sci.* 313, 677–686. <https://doi.org/10.1016/j.apsusc.2014.06.047>.
- Dougherty, C., 2011. *Introduction to Econometrics*. Oxford University Press.
- Fatima, R., Afridi, M.N., Kumar, V., Lee, J., Ali, I., Kim, K.-H., Kim, J.-O., 2019. Photocatalytic degradation performance of various types of modified TiO<sub>2</sub> against nitrophenols in aqueous systems. *J. Clean. Prod.* 231, 899–912. <https://doi.org/10.1016/j.jclepro.2019.05.292>.
- Fujishima, A., Honda, K., 1972. Electrochemical photolysis of water at a semiconductor electrode. *Nature* 238, 37–38.
- Grao, M., Amorim, C., Brito Portela Marcelino, R., Kelly, P., 2020. Crystalline TiO<sub>2</sub> supported on stainless steel mesh deposited in a one step process via pulsed DC magnetron sputtering for wastewater treatment applications. *J. Mater. Res. Technol.* 9, 5761–5773. <https://doi.org/10.1016/j.jmrt.2020.03.101>.
- Gupta, V.K., Jain, R., Mittal, A., Saleh, T.A., Nayak, A., Agarwal, S., Sikarwar, S., 2012. Photo-catalytic degradation of toxic dye amaranth on TiO<sub>2</sub>/UV in aqueous suspensions. *Mater. Sci. Eng. C* 32, 12–17. <https://doi.org/10.1016/j.msec.2011.08.018>.
- He, X., Wang, A., Wu, P., Tang, S., Zhang, Y., Li, L., Ding, P., 2020. Photocatalytic degradation of microcystin-LR by modified TiO<sub>2</sub> photocatalysts: a review. *Sci. Total Environ.* 743, 140694 <https://doi.org/10.1016/j.scitotenv.2020.140694>.
- Hu, Q., Liu, B., Zhang, Z., Song, M., Zhao, X., 2010. Temperature effect on the photocatalytic degradation of methyl orange under UV-vis light irradiation. *J. Wuhan Univ. Technol.-Materials Sci. Ed.* 25, 210–213. <https://doi.org/10.1007/s11595-010-2210-5>.
- Kelly, P.J., Arnell, R.D., 2000. Magnetron sputtering: a review of recent developments and applications. *Vacuum* 56, 159–172. [https://doi.org/10.1016/S0042-207X\(99\)00189-X](https://doi.org/10.1016/S0042-207X(99)00189-X).
- Lasa, H. de, Serrano, B., Salaices, M., 2005. *Photocatalytic Reaction Engineering*. Springer US.
- Montgomery, D.C., 2008. *Design and Analysis of Experiments*. John Wiley & Sons.
- Nguyen, T.T., Nam, S.-N., Son, J., Oh, J., 2019. Tungsten trioxide (WO<sub>3</sub>)-assisted photocatalytic degradation of amoxicillin by simulated solar irradiation. *Sci. Rep.* 9, 9349. <https://doi.org/10.1038/s41598-019-45644-8>.
- Ohsaka, T., Izumi, F., Fujiki, Y., 1978. Raman spectrum of anatase, TiO<sub>2</sub>. *J. Raman Spectrosc.* 7, 321–324. <https://doi.org/10.1002/jrs.1250070606>.
- Rueda-Marquez, J.J., Levchuk, I., Fernández Ibañez, P., Sillanpää, M., 2020. A critical review on application of photocatalysis for toxicity reduction of real wastewaters. *J. Clean. Prod.* 258, 120694 <https://doi.org/10.1016/j.jclepro.2020.120694>.
- Shams-Ghahfarokhi, Z., Nezamzadeh-Ejehieh, A., 2015. As-synthesized ZSM-5 zeolite as a suitable support for increasing the photoactivity of semiconductors in a typical photodegradation process. *Mater. Sci. Semicond. Process.* 39, 265–275. <https://doi.org/10.1016/j.mssp.2015.05.022>.
- Sundar, K.P., Kanmani, S., 2020. Progression of Photocatalytic reactors and it's comparison: a Review. *Chem. Eng. Res. Des.* 154, 135–150. <https://doi.org/10.1016/j.cherd.2019.11.035>.
- Tauc, J., Grigorovici, R., Vancu, A., 1966. Optical properties and electronic structure of amorphous germanium. *Physica Status Solidi B Basic Research* 15, 627–637. <https://doi.org/10.1002/pssb.19660150224>.
- Yamamoto, A., Mizuno, Y., Teramura, K., Shishido, T., Tanaka, T., 2013. Effects of reaction temperature on the photocatalytic activity of photo-SCR of NO with NH<sub>3</sub> over a TiO<sub>2</sub> photocatalyst. *Catal. Sci. Technol.* 3, 1771–1775. <https://doi.org/10.1039/C3CY00022B>.
- Yunus, N.N., Hamzah, F., So'aib, M.S., Krishnan, J., 2017. Effect of catalyst loading on photocatalytic degradation of phenol by using N, S Co-doped TiO<sub>2</sub>. *IOP Conf. Ser. Mater. Sci. Eng.* 206, 012092 <https://doi.org/10.1088/1757-899X/206/1/012092>.
- Zhao, Haoran, Qu, S., Guo, S., Zhao, Huiru, Liang, S., Xu, M., 2019. Virtual water scarcity risk to global trade under climate change. *J. Clean. Prod.* 230, 1013–1026. <https://doi.org/10.1016/j.jclepro.2019.05.114>.
- Zhu, J., Wang, X., Zhang, Q., Zhang, Y., Liu, D., Cai, A., Zhang, X., 2020. Assessing wetland sustainability by modeling water table dynamics under climate change. *J. Clean. Prod.* 263, 121293 <https://doi.org/10.1016/j.jclepro.2020.121293>.